Biogeochemical investigations of methane seepage at the ultraslow-spreading Arctic mid-ocean ridge: Svyatogor ridge, Fram Strait

C. Argentino [a,*], C. Borrelli [b], A. Akinselure [a], M. Correa-Diaz [b], G. Panieri [a]

[a] Department of Geosciences, The Arctic University of Tromsø, Tromsø, Norway
[b] Department of Earth and Environmental Sciences, University of Rochester, Rochester, NY, USA

ARTICLE INFO

ABSTRACT

The Arctic continental shelves are important reservoirs of methane stored in gas hydrates and deeper geological formations. However, little is known about methane dynamics in deeper oceanic settings such as mid-ocean ridges, mainly due to operational challenges related to their remoteness. This study investigates a recently discovered methane seepage environment at Svyatogor Ridge, a sediment-covered transform fault on the western flank of the Arctic mid-ocean ridge west of Svalbard. Svyatogor Ridge was previously hypothesized to host deep gas hydrates and active fluid flow systems, which is a unique combination for this setting and requires geochemical evidence. Based on sediment and foraminiferal geochemistry, we demonstrate that Svyatogor Ridge hosts a shallow methane cycle with anaerobic oxidation of microbial methane, sustaining chemosynthetic communities at the seafloor. Our geochemical datasets also suggest that methane fluxes were higher in the past than today and long-lasting, with episodes of intense methane oxidation recorded in pre-Holocene sediments. Methane seepage is still ongoing at this location, although no evidence exists that methane is reaching the sea surface. The results provide the first evidence of a methane seepage environment ever reported from the ultra-slow spreading Arctic mid-ocean ridge, thus calling for a reevaluation of the role of this type of ridge in the ocean methane cycle.

1. Introduction

Mid-ocean ridges (MOR) have played an important role in the ocean carbon cycling over the last 200 Myr (Wong et al., 2019). Magmatic heat transfer at oceanic spreading centres can influence the hydrocarbon maturation in the overlying sediment blankets and the geochemical evolution of fluids expelled at the seafloor (Berndt et al., 2016; Cruse and Seewald, 2006; Jakubowicz et al., 2021; Svensen et al., 2004). Phases of enhanced hydrothermal activity associated with elevated carbon dioxide (CO_2) emissions resulted in widespread benthic anoxia and mass extinctions (Cui et al., 2011; Zachos et al., 2005). Several studies have also advanced the hypothesis of a direct link between MOR activity and glacial cycles (Burley and Katz, 2015; Hasenclever et al., 2017; Huybers and Langmuir, 2009, 2017), caused by a sea-level forcing acting on magmatism and hydrothermal carbon fluxes. Those studies only considered CO_2 a major contributor to MOR-associated carbon emissions, but methane can also form and be emitted in these settings. In marine sediments, methane typically forms at temperature conditions compatible with microbial fermentation and carbonate reduction

pathways (microbial methane) (Zhuang et al., 2018), or via thermal cracking of organic molecules at higher temperatures (>80 °C) and pressures (2–4 km depth) (Selley and Sonnenberg, 2015) (thermogenic methane). Due to the high geothermal gradients in these regions and low inputs of organic matter available for methanogenesis, MOR are often unfavorable loci for significant methane generation via these two pathways. However, an abiotic path (methane non-deriving from organic matter) is also possible via serpentinization of ultramafic rocks (Etiope and Sherwood Lollar, 2013). This process is expected to occur at ultraslow-spreading ridges where seawater interacts with mantle rocks partially exposed at the seafloor (Konn et al., 2015; Welhan, 1988). It has been estimated that methane flux from MOR can contribute globally to up to 10 Mt/a, driven primarily by the slow and ultraslow spreading ridges in the Atlantic, Indian, and Arctic oceans, which is comparable to the flux from gas hydrates (2–9 Mt/a) (Merdith et al., 2020). Methane emissions at MORs are typically associated with warm hydrothermal fluids. Given the proportion of the Earth's mid-ocean ridge system (ca. 50%) spreading at slow-ultraslow rates (Sinha and Evans, 2004), these areas are potential targets for exploring and constraining this poorly

---

known source of methane and its cycling across the litho- and hydro-spheres. Finding seafloor evidence for methane-dominated seepage is challenging due to the difficulty in predicting the high-methane production MOR settings and the remoteness of these environments.

Visual observations of chemosynthetic fauna at the seafloor using remotely-operated vehicles can be used as a first-order indication of methane seepage. Still, similar communities can also be found at MOR in non-methane dominated settings, supported by high hydrothermal sulfide fluxes (Levin et al., 2016). Therefore, seafloor imagery shall be combined with pore fluid geochemistry and sediment-based proxies for methane oxidation to recognize methane seepage in a MOR context. In the sediments, methane is consumed by the consortia of archaea and bacteria, coupling methane oxidation with sulfate reduction (Boetius et al., 2000; Boetius and Wenzhöfer, 2013). This biogeochemical process occurs within a sediment interval called sulfate-methane-transition zone (SMTZ), conventionally centered at the interception between the methane and sulfate pore water concentration profiles. Where methane flux is high, the SMTZ is often very shallow, positioned at a few centimeters below the seafloor, and some methane can escape directly into the water column. The hydrogen sulfide flux released by sulfate-driven anaerobic oxidation of methane (AOM) sustains peculiar habitats relying on carbon fixation in the absence of sunlight (chemosynthesis). Those habitats have been widely reported in the literature and mainly consist of microbial mats, bivalves, and tubeworms and thrive on the products of AOM in the sediment underneath (Argentino et al., 2022a; Fischer et al., 2012; Sahling et al., 2002). The AOM process increases pore water alkalinity at the SMTZ and induces the precipitation of methane-derived authigenic carbonates (MDAC). These carbonates are easily identified as methane-derived owing to their $\delta^{13}C$ signature generally $< -30‰$ (Judd and Hovland, 2007). They record time-averaged information on biogeochemical processes spanning years to several millennia (Argentino et al., 2022b; Crémière et al., 2016; Feng et al., 2018; Himmler et al., 2019), while pore waters provide information over shorter timescales generally ranging from days to centuries (Hong et al., 2017; Klasek et al., 2021). MDAC can be dispersed as micro-scale concretions within the sediment or form large carbonate crusts partially exposed at the seafloor. Benthic and planktonic foraminiferal tests in the sediment are suitable templates for MDAC precipitation (Panieri et al., 2016, 2017). Their carbon and oxygen stable isotopes ($\delta^{13}C$ and $\delta^{18}O$) are among the most widely used proxies to reconstruct paleo-methane seepage (Consolaro et al., 2015; Dessandier et al., 2020, 2021; Millo et al., 2005; Panieri et al., 2012, 2016; Schneider et al., 2018; Yao et al., 2020). In particular, the benthic foraminifera $\delta^{13}C$ is traditionally interpreted to be evidence of the ability of these organisms to record the low $\delta^{13}C$ of dissolved inorganic carbon produced by methane oxidation (Kennett et al., 2000; Martin et al., 2010; Panieri et al., 2012; Rathburn et al., 2000; Sen Gupta et al., 1997) and/or the low $\delta^{13}C$ of methane-related food sources (Bernhard and Panieri, 2018; Panieri, 2006; Rathburn et al., 2003). However, several studies do not agree with this approach (e.g. Herguera et al., 2014; Torres et al., 2003a,b). Planktonic foraminifera do not typically record negative methane-derived $\delta^{13}C$ values in their tests in the water column. Still, when they die and sink into the sediment, they could be altered by MDAC, which precipitates on them. Indeed, both planktonic and benthic foraminiferal tests can be altered by the precipitation of MDAC around their shells, which alters their $\delta^{13}C$ signature towards very negative values, as negative as $-45‰$ (Consolaro et al., 2015; Martin et al., 2010; Panieri et al., 2016; Schneider et al., 2017; Torres et al., 2003a,b,2010).

In this study, we explore a methane seep environment located on an ultraslow-spreading mid-ocean ridge in the Arctic, Svyatogor Ridge (Fram Strait). Compared to other Arctic gas hydrate sites, Svyatogor Ridge is particularly interesting because it is located on an active ultraslow-spreading ridge that hosts gas hydrates potentially charged by abiotic methane (Johnson et al., 2015; Waghorn et al., 2020). We visited

Svyatogor Ridge during a recent oceanographic expedition (Bünz and Panieri, 2022) with an ROV onboard, allowing for high-resolution seafloor observations and targeted sediment samplings via push coring and blade coring. We also collected gravity cores, providing a longer sedimentary record. Here, we studied present-day and past methane dynamics by applying a multiproxy approach that included pore water geochemistry (sulfate and dissolved inorganic carbon-[DIC] concentration; DIC isotopic composition), headspace gas composition, sediment geochemistry (total organic carbon, total nitrogen, and their isotopic compositions) and X-Ray fluorescence chemical analyses on the gravity cores. The results provide the first evidence of methane seepage ever reported from the Arctic mid-ocean ridge, thus calling for a reevaluation of the role of ultraslow-spreading ridges in the ocean methane cycle.

2. Study area and geological setting

Svyatogor Ridge is an elongated, sedimented ridge located on the northwestern flank of the Knipovich Ridge and south of the Molloy Deep (Fig. 1)(Waghorn et al., 2018, 2020). The Svyatogor Ridge sits about 80 km south of Vestnesa Ridge, a large contourite deposit extending off the continental margin to the west of Svalbard. Originally, both ridges were part of the same complex until they were separated by transform faulting (Johnson et al., 2015). Movement on previously sedimented detachment faults resulted in the formation of sedimentary faults on Svyatogor Ridge. Although it was initially considered an inactive area of methane seepage (Johnson et al., 2015), it is now recognized that this ridge hosts extensive gas hydrates and underlying free gas system as well as fluid flow systems (Waghorn et al., 2018, 2020). Differently from the other gas hydrate systems in the Fram Strait, e.g. Vestnesa Ridge and Western Svalbard Margin, Svyatogor Ridge is an actively rifting environment (Waghorn et al., 2018). Waghorn et al. (2020) suggested that abiotic methane may contribute to the gas hydrate system on the western Knipovich Ridge flank of the Svyatogor Ridge, with faults along this ridge acting as conduits for fluid migration. Chimneys and pockmarks are also present (Riedel et al., 2020).
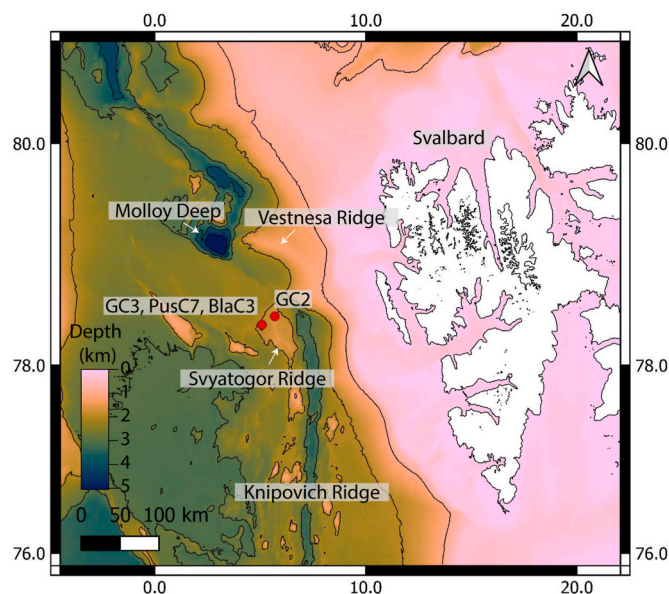

Fig. 1. IBCAO (International Bathymetric Chart of the Arctic Ocean) topographic map showing the sampling sites at Svyatogor Ridge, Arctic Ocean. PusC7 and BlaC3 are located 1 m away from each other and ~25 m to the East of GC3. GC2 is located at ~16 km from GC3, PusC7, and BlaC3 area (also summarized in Table 1).

3. Methods

3.1. Coring

For this study, we utilized sediment samples from two gravity cores (CAGE21-1-KH04-GC2 of length 315 cm and CAGE21-1-KH04-GC3 of length 214 cm), one push core (CAGE21-1-KH04-Dive06-PusC7), and one blade core (CAGE21-1-KH04-Dive08-BlaC3) (Fig. 1), hereafter named GC2, GC3, PusC7 and BlaC3, respectively (Table 1). These cores were collected during the CAGE21_1 (AKMA1) cruise onboard the RV Kronprins Håkon (Bünz and Panieri, 2022).

The gravity cores were collected using a 6-m-long corer deployed from a side of the vessel using a crane. The corer hosted a plastic liner and was closed at the bottom with a core catcher to avoid sample loss and a cutter to facilitate penetration at the seafloor. After recovery, the gravity cores were cut into 100 cm sections, and kept at 5 °C on board. Seafloor imagery acquired with the remotely operated vehicle Ægir 6000 ROV revealed the presence of white microbial mats and tubeworms, associated with black reduced sediment (Fig. 2a). Microbial mats locally reach over 1 m in width (Fig. 2b). The push core and the blade core were collected with the ROV from a background non-seep-impacted seafloor (Fig. 2c) and from a microbial mat and tubeworm habitat (Fig. 2d), respectively.

Bulk sediment samples for headspace gas analysis were collected from the bottom of GC2, GC3, PusC7 and a core collected from a microbial mat in the same seepage area during a previous dive CAGE21-KH04-Dive05-PusC3 (PusC3). The samples were fixed with 1 M NaOH and stored at 5 °C. The push and blade cores were sliced onboard at 1 cm intervals, and the samples were kept at 5 °C. Gravity cores were core logged and then sampled at the onshore facilities in the Geology Laboratory, UiT The Arctic University of Norway (Tromsø, Norway). Samples were collected every 10 cm. A total of 58 samples were retrieved from the gravity cores and 63 samples from the push and blade cores. Samples were freeze-dried prior to chemical treatments and analyses.

3.2. Core logging

Core logging was conducted on the two gravity cores at the Geology Laboratory (UiT) in Tromsø. Magnetic susceptibility (MS) was measured at 1 cm intervals using a GeoTek Multi-Sensor Core Logger (MSCL-S) system. Geochemical datasets were acquired at 1 cm resolution using an Avaatech X-Ray Fluorescence (XRF) Core Scanner. Elements were quantified at 10 kV (1000 mA, no filter, and 10 s measuring time per step), 30 kV (2 mA, Pd-thick filter, and 20 s measuring time per step), and 50 kV (same setting as the ones used for 30 kV, with Cu-filter for barium). The raw data was processed using the WinAxil program. This study used elemental ratios (X/Ti, where X is the target element) rather than single-element intensities to minimize matrix effects (Hennekam

Table 1
Location of coring sites and sediment recovery. Comments are based on ROV observations and water-column data (methane flares).

Core	Coordinates (DD)	Water depth (m)	Recovery (cm)	Comments
PusC7 (Push core)	78.3925°N 5.0834°E	1928	37	Reference core within seep area
BlaC3 (Blade core)	78.3925°N 5.08346°E	1929	21.5	Presence of microbial mat and tubeworms
GC3 (Gravity core)	78.3924°N 5.0825°E	1893	208	Core within seep area
GC2 (Gravity core)	78.4738°N 5.6891°E	1671	313	Reference core outside seep area
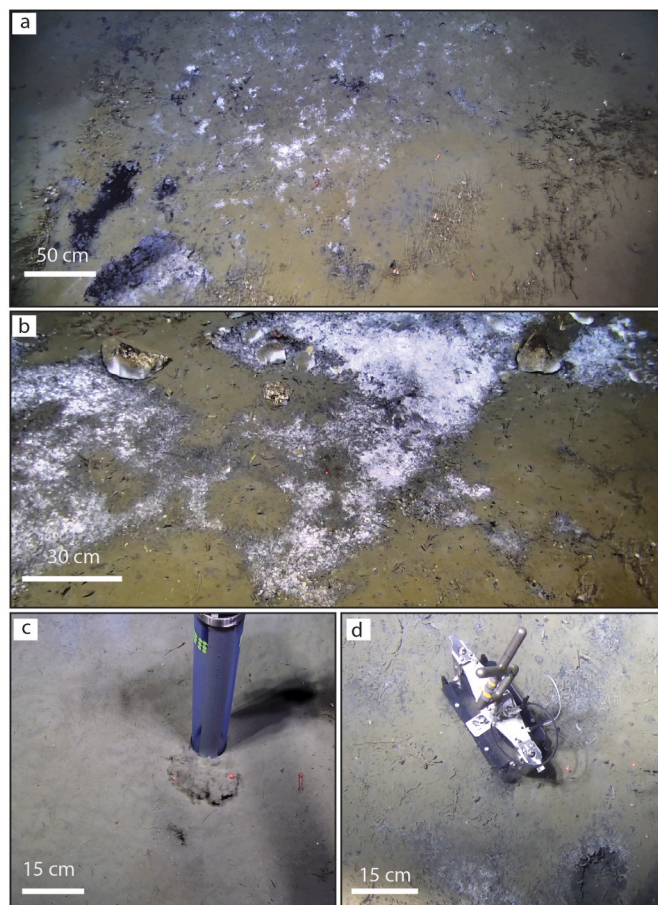
Fig. 2. Seafloor images from the seepage area showing the microbial mats and tubeworm habitats; the sediment below the surface is marked by reducing conditions as indicated by its black color (a). Microbial mats observed in the study area range from a few tens of cm in width to over 1 m (b). ROV picture of the (c) push core PusC7 and (d) blade core BlaC3 collected during CAGE21-1-AKMA1 cruise (Bünz and Panieri, 2022).

and De Rick, 2012). In this study, we focused on Ca/Ti, Zr/Rb, Ba/Ti and Fe/Ca ratios as proxies for carbonate content, grain size (Zr resides mainly in coarser grains and Rb in clays), barite content and terrigenous inputs (Fe in detrital clay: Ca in carbonates), respectively (Rothwell and Croudace, 2015). It is worth mentioning that plagioclase content in deep-sea sediments of the Fram Strait is generally low (Maslov et al., 2023), so we can assume that Ca variations in our pelagic cores reflect carbonate content. These proxies are used in addition to MS to support the lithostratigraphic correlations between GC2 and GC3 (Rothwell and Croudace, 2015; Wu et al., 2020) and investigate the geochemical record of authigenic minerals associated with modern or paleo-SMTZs (Argentino et al., 2021; Johnson et al., 2021; Schneider et al., 2018; Yao et al., 2020). Lithological units identified based on XRF and MS datasets were used for palaeoceanographic constraints and age models. The chronostratigraphic approach was established by identifying the main lithostratigraphic units in relation to the Late Weichselian ice age, which began about 115,000 years ago and ended 11,700 years ago (Lucchi et al., 2013). Particular attention was devoted to finding evidence of sediment deposition by meltwater plumes and icebergs, affecting the sediment organic matter inventory (marine vs terrestrial inputs).

3.3. Total organic carbon (TOC), total nitrogen (TN) and their isotopic signature ($\delta^{13}C$, $\delta^{15}N$)

The carbon and nitrogen geochemical analyses were conducted on

bulk sediment samples from GC3, PusC7, and BlaC3 to investigate the sources of organic matter in the seepage area. For this reason, GC2 was not included in these analyses. Sample preparation and analysis are briefly summarized here. For each sample, roughly 3–4 g of sediment was treated with 5 mL 6 M HCl to dissolve the carbonate fraction. Samples were dried at 50 °C, weighed in tin capsules, and analyzed on a Thermo-Fisher MAT253 Isotope Ratio Mass Spectrometer (IRMS) coupled to a Flash HT Plus Elemental Analyzer. Carbon and nitrogen stable isotope values (δ^{13}C and δ^{15}N) results are reported relative to the Vienna Pee Dee Belemnite (VPDB) standard for carbon and atmospheric air for nitrogen. Analytical precision was estimated to be better than ±0.07‰ for both carbon and nitrogen. The repeatability of duplicate samples for TOC, TN, δ^{13}C and δ^{15}N was 0.25%, 0.03%, 1.46‰, and 0.87‰, respectively. The atomic mass-weighted ratio of total organic carbon (TOC) and total nitrogen (TN) was used to compute the C/N atomic ratio, calculated as C/N = (TOC/12.011)/(TN/14.007).

3.4. Pore fluid chemistry (sulfate, dissolved inorganic carbon – DIC, gas)

Pore water samples were extracted onboard immediately after core recovery. The pore water was filtered out of the sediment cores using Rhizon samplers and 10 mL sterile syringes. Samples were split in two aliquots: (1) for sulfate analysis (2) for DIC analysis. Aliquot (1) was kept frozen at −20 °C, whereas aliquot (2) was kept in the dark at 5 °C until the analysis. The sulfate concentration was measured at TosLab AS in Tromsø via Ion Chromatography. Pore water was not extracted from GC2. Repeated measurements of in-house and international standards were used to check accuracy and precision during the analyses; measured values agree with the certified value within the associated uncertainty. Dissolved inorganic carbon (DIC) and its isotopic signature (δ^{13}C) were measured at Stable Isotope Laboratory-SIL at UiT on a MAT253 IRMS coupled to a Gasbench II with analytical precision better

than ± 0.15‰. Methane concentration in headspace gas samples was measured at SIL-UiT using a ThermoScientific Trace 1310 gas chromatograph. Methane isotope composition (δ^{13}C) was measured using a Nu Horizon (Nu Instruments Ltd., UK) at IFE, Institute for Energy Technology (Oslo, Norway). Calibration was done with in-house standards. Precision on δ^{13}C was estimated as 0.5‰ VPDB (1SD).

3.5. Micropaleontology

For each sample, 50–60 gr of sediment were weighed and wet-sieved using 63 and 125 μm sieves. Residues were dried at 50 °C. Benthic and planktic foraminifera were picked using a stereomicroscope from the fraction >125 μm and identified to species level prior to isotopic analysis. Due to their abundance in the samples analyzed, *Neogloboquadrina pachyderma* (planktonic species) and *Cibicides wuellerstofi* (benthic species) were selected for analysis. Five to 15 specimens from each samples were measured for δ^{13}C and δ^{18}O using a Thermo Fisher MAT253 IRMS with a Gasbench II hosted at SIL, Stabe isotope Laboratory at UiT. Analytical precision was estimated to be better than ±0.08‰ for oxygen and ±0.03‰ for carbon. All isotope results were reported to standard delta notation relative to VPDB.

4. Results

4.1. Magnetic susceptibility (MS)

The MS measured on the gravity core GC3 shows the lowest value of 3.30 SI x 10^5 at 66 cm depth and the highest value of 41.34 SI x 10^5 at 97 cm depth (Fig. 3a). There was a gradual increase in MS from the top of the core to about 52 cm below the seafloor (bsf) and from 67 cm to 100 cm. The MS started decreasing in values from 53 cm to 66 cm, and from 101 cm to 107 cm depth. MS values fluctuated between 9.92 SI x 10^5 and
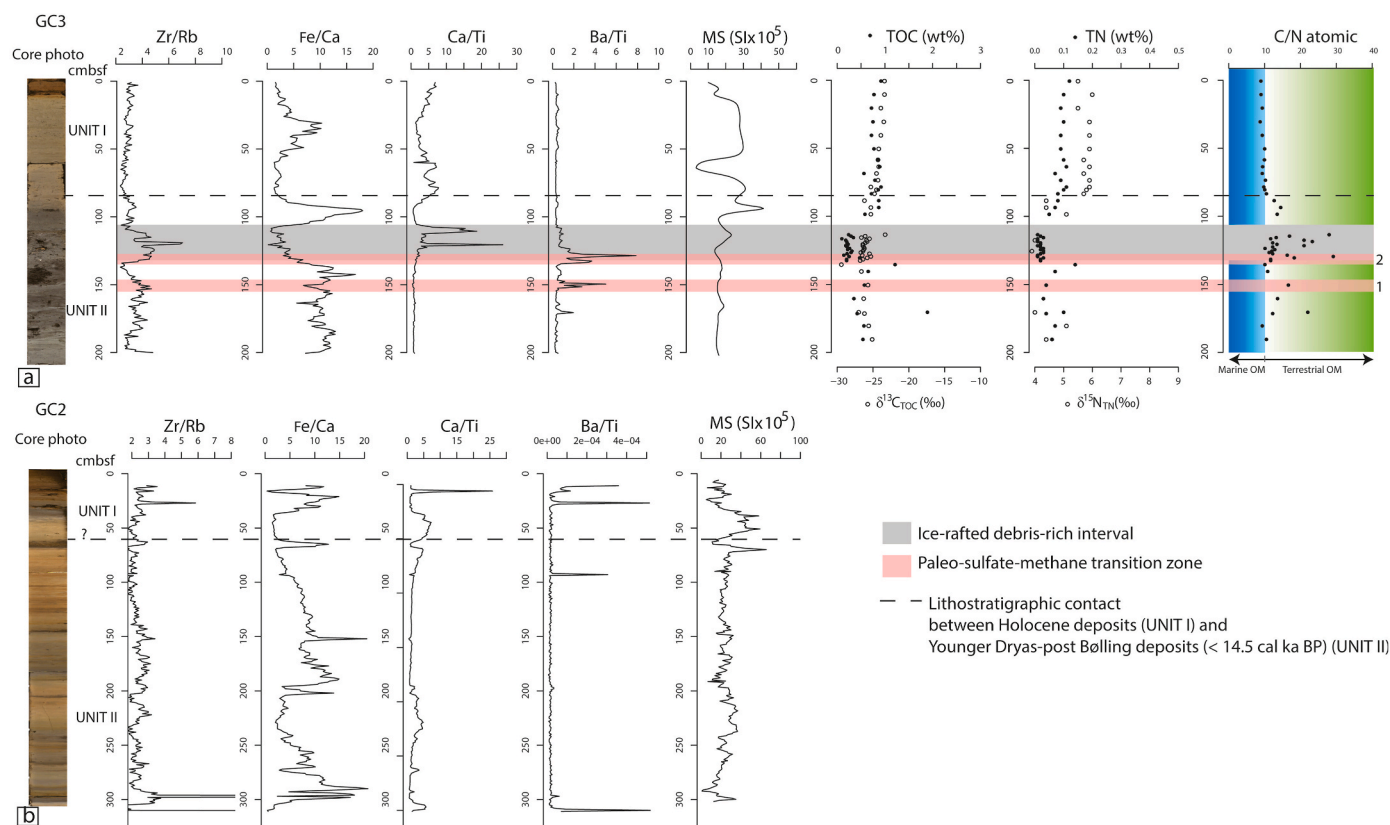
Fig. 3. Photo, X-Ray Fluorescence data and magnetic susceptibility (MS) for gravity cores GC3 (a) and GC2 (b); total organic carbon (TOC), total nitrogen (TN), and carbon-nitrogen systematics of GC3 (a). C/N value 10 is marked as the upper threshold for marine organic matter (Meyers, 1994).

23.00 SI x 10⁵ from the depth of 116 cm–214 cm. The MS measured on gravity core GC2 has the highest value of 65.67 SI x 10⁵ at depth 82 cm, with an intermittent increase at depths 51 cm, 63 cm, and 311.9 cm (Fig. 3b).

4.2. X-Ray Fluorescence (XRF)

The Zr/Rb ratio measured in gravity core GC3 shows a uniform trend between the top of the core and 58 cmbsf (Fig. 3a). There is an increase in peak between the depths of 121 cm and 140 cm, with the highest peak at depth 128 cm. The Zr/Rb ratio measured in gravity core GC2 shows a rather uniform trend throughout the core, with two isolated peaks at depths of 287 cm and 301 cm (Fig. 3b). In gravity core GC3, the Fe/Ca ratio shows high values at around 35 cmbsf, a prominent peak at ~90 cm, and rather steadily high values below 140 cm (Fig. 3a). In gravity core GC2, the Fe/Ca values show higher contents in the uppermost 40 cm, between 100 cm and 200 cm and from 250 cm downcore (Fig. 3b). An isolated peak is observed at 60 cm. The Ca/Ti ratio measured in gravity core GC3 shows a decreasing trend from the top of the core to ~32 cmbsf before it begins to increase (Fig. 3a). It shows a dramatic increase at depths 119 cm and 129 cm. Within this interval, a shell-rich layer is also observed. Ca/Ti decreases at depths 60 cm, 105 cm, and 153 cm. There is no significant change in the proportion of the two elements from depth 160 cm downward. On the other hand, the Ca/Ti ratio of the gravity core GC2 shows almost a uniform trend throughout the core except for a significant peak at a depth of 6 cm (Fig. 3b). The Ba/Ti ratio measured in gravity core GC3 shows a uniform trend throughout the core except for significant peaks clustering around the depths 137 cm, 157 cm and 178 cm (Fig. 3a). In the gravity core GC2, it shows a uniform trend with sporadic isolated peaks intermittently at 15 cm, 28 cm, 90 cm and 314 cm (Fig. 3b).

4.3. Carbon and nitrogen systematics (TOC, TN, $\delta^{13}C$, $\delta^{15}N$)

A total of 117 sediment samples were analyzed from GC3, PusC7, and BlaC3 to explore the sources of organic matter in the sediments collected. For gravity core GC3 (Fig. 3a), the $\delta^{13}C_{TOC}$ values range between −29.4‰ and −23.3‰, and the $\delta^{15}N$ values between 1.7‰ and 6.0‰. TOC (wt %) values fluctuate between 0.10 and 1.89, the TN (wt %) values are between 0.01 and 0.14, and the C/N ratio varies between 8.7 and 29.2. In push core PusC7 (Fig. 4a), the $\delta^{13}C_{TOC}$ values range

between −27.3‰ and −23.2‰ and the $\delta^{15}N$ values between 4.1‰ and 5.9‰. The TOC (wt%) values vary between 0.24 and 0.80, the TN (wt %) values between 0.03 and 0.11, and the C/N ratio between 8.0 and 12.5. In blade core BlaC3 (Fig. 4b), the $\delta^{13}C_{TOC}$ values range between −32.4‰ and −25.4‰ and the $\delta^{15}N$ values between 1.2‰ and 4.8‰. The TOC (wt %) values vary between 0.18 and 0.68, the TN (wt %) between 0.02 and 0.08, and the C/N ratio between 7.8 and 14.8.

4.4. Pore fluids and foraminifera geochemistry

Pore water sulfate concentration profiles are used to determine the depth of the SMTZ, the redox zone of the sediment in which methane oxidation takes place anaerobically (e.g. Hensen et al., 2003; Kasten et al., 2003). Below the SMTZ, there is no further detectable decrease in downcore sulfate concentration. The SMTZ is also typically associated with high DIC concentrations and decreasing $\delta^{13}C$ values due to methane-derived carbon released into pore waters during AOM. Gravity core GC3 shows a near-zero sulfate concentration gradient (Fig. 5a), stable at seawater concentration of ~28 mM. DIC values range between of 2.5 mM and 3.1 mM. associated with $\delta^{13}C$ between −5.0‰ and −1.6‰. Headspace methane concentration at the bottom of the core is < 0.01 mM. In this core, planktonic foraminifer *Neogloboquadrina pachyderma* shows $\delta^{13}C$ values ranging between −2.33‰ and 0.73‰ and $\delta^{18}O$ values between 1.36‰ and 5.00‰ (Fig. 5a). In case of the benthic species *Cibicides wuellerstofi*, the $\delta^{13}C$ values ranges between −12.73‰ and 1.26‰ and $\delta^{18}O$ values between −0.53‰ and 4.84‰. In gravity core GC2, the planktonic foraminiferal $\delta^{13}C$ oscillates between −0.16‰ and 0.73‰, whereas the $\delta^{18}O$ ranges between 3.09‰ and 4.89‰ (Fig. 5b). Headspace methane concentration at the bottom of GC2 is < 0.01 mM.

In push core PusC7, sulfate concentration shows no trends, with values stable at around 28 mM (Fig. 5c). DIC isotopic composition shows values between −8.0‰ and −3.4‰. Methane concentration in the sediment is 0.21 mM, slightly higher than in the gravity cores. The $\delta^{13}C$ value of methane in the same sample is −60.1‰. In PusC3 (push core from the same seepage area), the methane concentration is 0.03 mM and $\delta^{13}C$ of methane is −85.0‰. *N. pachyderma* $\delta^{13}C$ and $\delta^{18}O$ oscillate as depth increases. Specifically, $\delta^{13}C$ values ranges between −0.15‰ and 0.62‰ and $\delta^{18}O$ ranges between 0.77‰ and 3.50‰ (Fig. 5c). *C. wuellerstofi* recorded an opposite trend for $\delta^{13}C$ and $\delta^{18}O$ at 6–7 cm, 38–39 cm and 40–41 cm. The trend becomes similar at 25–26 cm and 31–32

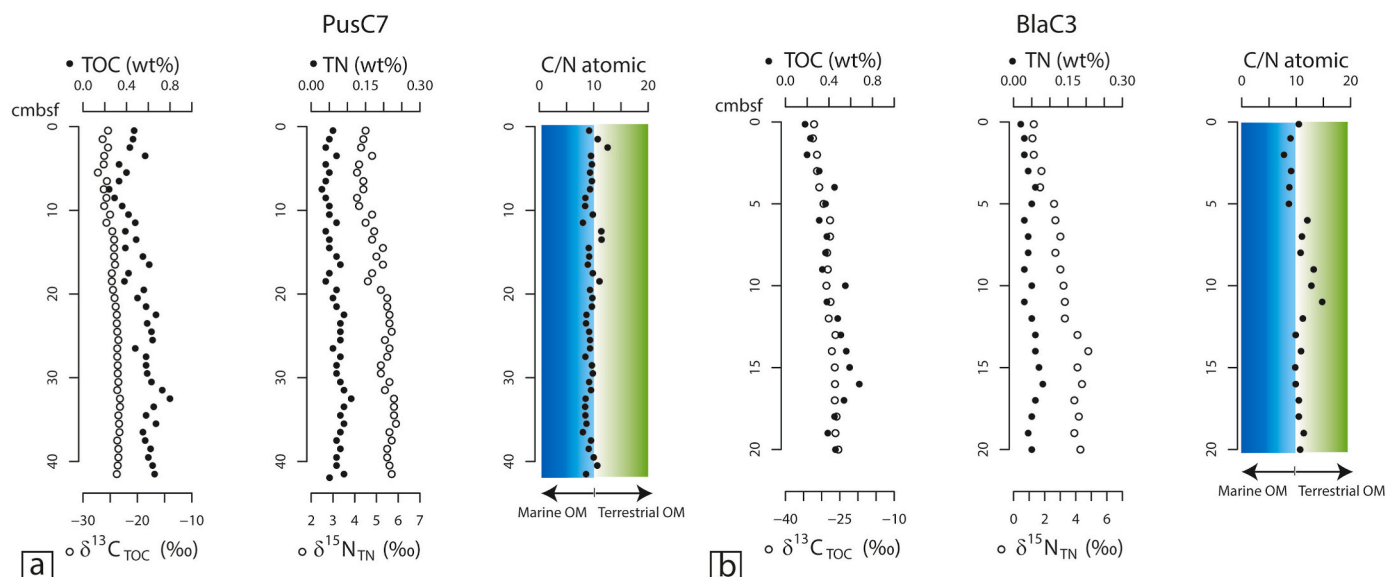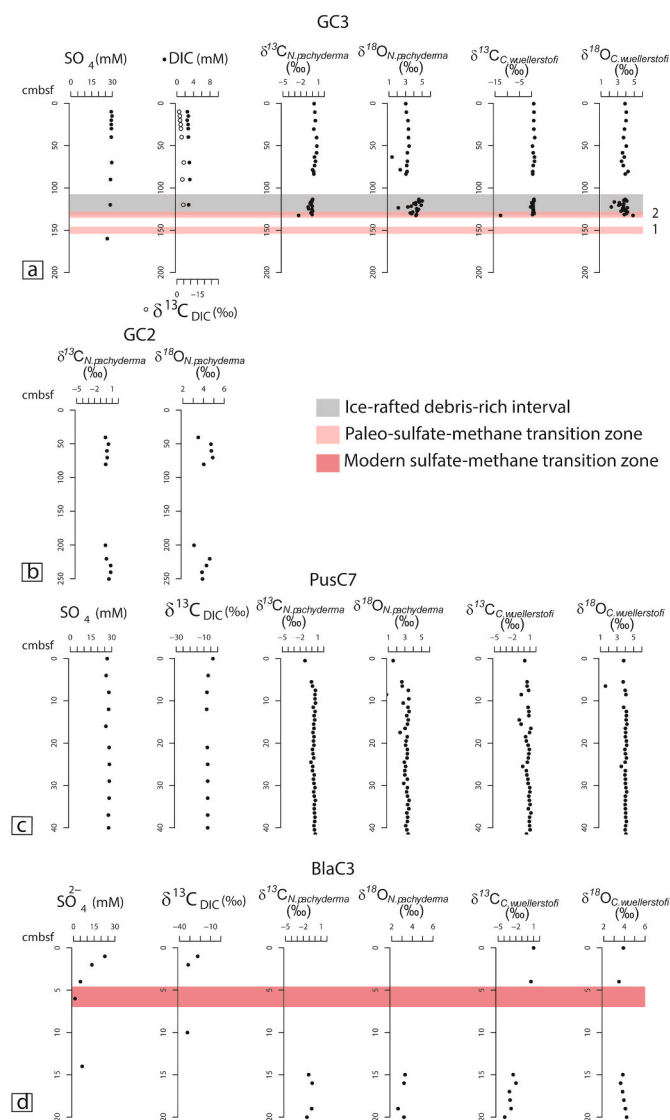**Fig. 4.** Total organic carbon (TOC), total nitrogen (TN), and their isotopic composition ($\delta^{13}C_{TOC}$, $\delta^{15}N_{TN}$) in cores PusC7 (a) and BlaC3(b). A C/N value of 10 is marked as the upper threshold for marine organic matter (Meyers, 1994).

Fig. 5. Sulfate, dissolved inorganic carbon (DIC), dissolved inorganic carbon stable carbon isotopes (δ^{13}C), and planktonic and benthic foraminiferal carbon and oxygen stable isotopes ($\delta^{13}C_{N.\ pachyderma}$, $\delta^{13}C_{C.wuellerstorfi}$, $\delta^{18}O_{N.\ pachyderma}$, $\delta^{18}O_{C.wuellerstorfi}$) profiles for sediment cores GC3 (a), GC2 (b), PusC7 (c) and BlaC3 (d). Intervals with no foraminifera data represent sediment that was barren of the targeted foraminiferal species used in this study.

cm. The δ^{13}C ranges between −0.81‰ and 1.17‰ and the δ^{18}O between 1.60‰ and 4.18‰ (Fig. 5c).

The sulfate concentration profile in BlaC3 shows a concave down shape with almost complete depletion at 6 cm (1.2 mM) (Fig. 5d). The sample at 14 cm is characterized by a higher value compared to the sample at ~6 cm, but this could be due to intrusion of fresh seawater at the bottom of the blade core. DIC has an isotopic composition highly depleted in ^{13}C, with values from −32.2‰ to −22.3‰. The DIC δ^{13}C signature becomes more negative downcore, matching the trend of the sulfate concentration profile (Fig. 5d). *N. pachyderma* δ^{13}C ranges between −1.36‰ and −0.51‰ and δ^{18}O between 2.62‰ and 3.30‰ (Fig. 5d). *C. wuellerstofi* δ^{13}C values are between −3.94‰ and 0.98‰ and δ^{18}O values between 3.48‰ and 4.22‰ (Fig. 5d).

5. Discussion

5.1. Lithostratigraphy

The sediment core GC3 can be divided into two units (here 'unit' defined as a volume of sediment with homogenous properties and a relative age range) based on sediment properties such as grain size (Zr/Rb ratio), carbonate content (Ca/Ti ratio and visual observation of bivalve shells), organic geochemistry (C/N atomic ratio) and terrigenous inputs (Fe/Ca ratio). Interestingly, the latter proxy shows a change in signal intensities (from relatively high to relatively low values; from sedimentation dominated by terrestrial debris inputs to sediments dominated by marine biogenic debris) also corresponding to change in sediment color as shown by XRF imagery (Fig. 3a). Unit I (0–83 cm) is rich in sandy mud and brownish in color. In Unit I, the δ^{13}C values of organic matter are mostly comprised between −24‰ and −22‰, and δ^{15}N values are rather stable around an average value of 6‰ (Fig. 3A). Marine organic carbon typically shows $\delta^{13}C_{TOC}$ values between −23‰ to −16‰ (Emerson and Hedges, 1988; Meyers, 1994), whereas terrestrial sources have lighter values compared to marine sources, with Arctic end-members generally in the window between −27‰ and −26‰ (Knies and Martinez, 2009). The nitrogen isotopic composition of marine organic matter is heavier than terrestrial organic matter, the former reaching values as high as 6–7‰ whereas land-derived organic matter is characterized by values close to 1‰ (Kienast et al., 2005; Wada, 1980). Therefore, we conclude that Unit I was deposited during open marine conditions with predominant inputs of marine organic matter. This is also confirmed by the C/N ratios mostly lower than 10, which is the threshold value separating marine (lower values) from terrestrial (higher values) sources (Emerson and Hedges, 1988; Meyers, 1994). The Ca/Ti ratios are generally higher and Fe/Ca lower in this unit compared to the underlying sediments. Ca/Ti is a proxy for calcium carbonate content, deriving from authigenic or biogenic material (Rothwell and Croudace, 2015). The Fe/Ca ratio reflects the terrigenous vs biogenic sediment inputs (clay/carbonate content ratio) (Rothwell and Croudace, 2015). Based on those data, we ascribed Unit I to have deposited during the Holocene (starting around ~11.7 cal ka BP). Unit II (83–214 cm) consists of dark grey silty mud and fine-grained sand. There appears to be ice-rafted debris (IRDs; sediments of varying grain sizes carried by floating ice and dropped into any aqueous environment) lodged in the gravity core, as well, which could be responsible of the increase in Zr/Rb ratios reflecting higher grain size (Wu et al., 2020) between depths 120 and 140 cm (Fig. 3a). A shell layer is also present and corresponds to the highest Ca/Ti peak at 129 cm. Shells are fragmented and/or disarticulated, and have not been classified. The bivalve shells seem to have been reworked and deposited alongside the pebbles by icebergs. This interval has the highest C/N values, ranging between ~22 and ~29, and the lowest isotopic values ($\delta^{13}C_{TOC}$, δ^{15}N), demonstrating enhanced terrestrial inputs of organic matter. The total organic content is remarkably low in this interval, diluted by inorganic sediment particles. Unit II is barren in foraminifera from 134 to 214 cm. This, together with the presence of IRDs and sporadic sandy laminae, suggests that Unit II was deposited in a seasonally deglaciated sea ice setting, which resulted in the settling of fine-grained sediments and lower biological activity (Eynaud, 2011). This unit is ascribed to a depositional phase within the Late Weichselian deglaciation, likely the Younger Dryas-post Bølling period (<14.5 cal ka BP).

Gravity core GC2 consists of a fine-grained laminated unit. Laminae-scale color changes are frequent. Dark laminae are associated with spikes in Fe/Ca values and drops in Ca/Ti and magnetic susceptibility. These geochemical observations are interpreted as enrichments in paramagnetic iron sulfide content, i.e., pyrite and low biogenic carbonates. This might indicate a periodic low oxygen environment at the seafloor, favoring pyrite formation and preservation and low biological activity. The scattered Zn/Rb profile and laminated features suggest turbiditic inputs. The sediments in GC2 look different than GC3, possibly

due to the different depositional setting, i.e., on a gentle slope of a ridge vs on the crest of a ridge, and the subdivision into lithostratigraphic units is challenging. However, some lines of correlation can be tentatively drawn using the XRF data and magnetic properties. The bulges in Fe/Ca at 20–40 cm and Ca/Ti at 25–50 cm in GC2 seem to match the bulges at 20–50 cm and 60–100 cm in GC3. In both cores, these features are associated with higher magnetic susceptibility followed by a decrease in signal intensity. This would imply that the contact between Unit I (Holocene) and Unit II (Younger Dryas-post Bølling) is at ~ 60 cm. The sediment geochemistry of PusC7 reveals a marine-dominated organic matter. BlaC3 shows an overall marine-derived source for the organic matter although the uppermost 5 cm of sediments have isotopic values not consistent with marine and terrestrial inputs and will be further discussed in the next chapter. Overall, the shorter cores are in agreement with Unit I being deposited in the Holocene.

The oxygen isotopic composition of foraminifera can further support the paleo-environmental interpretations of the investigated cores. The $\delta^{18}O$ values of *N. pachyderma* measured from GC3, GC2, PusC7, and BlaC3 range between 0.77 and 5‰. $\delta^{18}O$ values as low as 2.8-3‰ were measured in *N. pachyderma* sin from Vestnesa Ridge in Post-Last Glacial Maximum (17.8-16.7 ka BP) sediments and in sediment from the Fram Strait during the Last Glacial Maximum (23.5–24 ka BP) (Elverhøi et al., 1995; Schneider et al., 2018). Based on the similarity of the *N. pachyderma* sin $\delta^{18}O$ values measured in this study with the $\delta^{18}O$ values measured in sediments from Vestnesa Ridge and Fram Strait, we interpret our record as an indication that the sediment from gravity cores and the blade core analyzed were deposited during the last deglaciation. Also, low $\delta^{18}O$ values could indicate melt-water contributions from the Svalbard-Barents Sea Ice Sheet (SBIS), which could be seen across the North Atlantic (Elverhøi et al., 1995; Schneider et al., 2018).

5.2. Biogeochemical evidence of anaerobic oxidation of methane

The down-core variation of pore water sulfate concentration is essential to identify the depth of the modern SMTZ (e.g. Hensen et al., 2003; Kasten et al., 2003). On the other hand, the solid-phase geochemistry of the sediment includes all the anomalies generated by methane oxidation through time. Combining pore water and sediment geochemistry in different cores is an effective approach to reconstruct seepage dynamics through time (Argentino et al., 2021; Schneider et al., 2018; Yao et al., 2020), overcoming the challenges related to the extreme temporal and spatial heterogeneity of cold seepage environments (Ferré et al., 2020). The occurrence of ^{13}C-depleted carbonates is a common proxy for AOM (Argentino et al., 2022b; Crémière et al., 2016; Himmler et al., 2019; Judd and Hovland, 2007; Roberts and Feng, 2013) since it reflects the direct incorporation of methane-derived carbon released into pore water upon oxidation. Several other indicators, such as the enrichment of barium in narrow stratigraphic intervals at the top of SMTZs, generated by barite precipitation at the interception of sulfate- and barium-rich waters (Carter et al., 2020). The hydrogen sulfide released by sulfate-dependent AOM tends to form iron sulfide accumulations which can be tracked by monitoring magnetic susceptibility anomalies along the sediment cores (Johnson et al., 2021). These proxies were used by Schneider et al. (2018) to identify shallow subseafloor diagenesis and episodes of past seafloor methane seepage along Vestnesa Ridge since the Last Glacial Maximum (LGM) and during the retreat of the Svalbard-Barents Sea Ice Sheet (SBIS) as well as by other authors at Arctic cold seeps (Argentino et al., 2021; Yao et al., 2020). In GC3 and PusC7, the sulfate profiles demonstrate that there is no SMTZ within the sampled sediment intervals (Fig. 3a; 5a, c). This agrees with the fact that GC3 was collected from a reference area outside the seep zone, and PusC7 was collected from a reference area within the seep (i. e., an area without any evidence of seep habitats at the seafloor). Sediments at sites characterized by high methane fluxes and shallow SMTZs are typically colonized by microbial mats and tubeworms thriving on the

sulfide released by AOM (Argentino et al., 2022b; Fischer et al., 2012; Sahling et al., 2002). Both GC3 and PusC7 have negligible methane concentrations, in agreement with the flat sulfate and DIC pore water profiles. Differently, BlaC3 displays an SMTZ at around 6 cm (Fig. 2b; 5d). The DIC $\delta^{13}C$ and concentration support the presence of such shallow SMTZ, in which methane oxidation produces ^{13}C-depleted bicarbonate ions. The isotopic composition of organic matter in the uppermost sediment layer hosting the microbial mat (Fig. 4B) yielded $\delta^{13}C$ values as negative as −32.4‰, confirming that it's mostly composed of chemoautotrophic organisms, typical of cold seep environments (Gilhooly et al., 2007; Heijs et al., 2005). Considering the isotopic effect of −25‰ (Ruby et al., 1987) associated with that trophic strategy, the main carbon source for the microbial mats is DIC from seawater, with a minor contribution from methane-derived carbon in the pore waters. This interval also shows low $\delta^{15}N$ values compared to the rest of the core and the other cores. The negative isotope excursions observed in BlaC3 are found in other mats from cold seeps (Gilhooly et al., 2007; Grünke et al., 2012) and might reflect nitrogen uptake via ammonium assimilation, nitrate reduction (Hoch et al., 1992; Macko et al., 1987) or nitrogen fixation (Nelson et al., 1982). GC3 and PusC7 have low DIC concentration and a slightly negative $\delta^{13}C$ signature generated by organic matter respiration releasing DIC with isotopic composition ~ $\delta^{13}C_{TOC}$, between −29‰ and −23‰, which mixes with seawater DIC of ~0‰. The C/N ratios in all the cores show a predominant marine component with few intervals marked by enhanced terrestrial inputs linked to the activity of icebergs. In BlaC3, the low C/N values in the uppermost 5 cm are likely influenced by the presence of bacterial biomass, which has values as low as 4 (Madigan et al., 2017). We do not have pore water data for GC2, so we cannot track the depth of the present-day SMTZ. However, the methane concentration in this core is lower than 0.01 mM, which clearly indicates that the SMTZ and the methanogenic zone are located deeper than the investigated interval. The $\delta^{13}C$ values of *N. pachyderma* sin and *C. wuellerstofi* from GC3 (Fig. 5a), GC2 (Fig. 5b), and PusC7 (Fig. 5c) show normal marine signatures (from −1‰ to +1‰; Ravelo and Hillaire-Marcel, 2007), thus indicating that the foraminiferal shells were not affected by AOM-derived carbonate overgrowth (Panieri et al., 2017). The only exception is the sample collected from GC3 at 132 cm, which shows a remarkably negative $\delta^{13}C$ value of −12.73‰, produced by secondary overgrowth of methane-derived carbonate. BlaC3 was barren of foraminifera except for narrow intervals, which do not show AOM influence (Fig. 5d). Ca/Ti profiles from XRF logging of gravity cores agree with the foraminiferal observations, as there are no intervals with prominent carbonate enrichments related to methane-derived carbonate concretions precipitating on the foraminifera shells. Therefore, the Ca distribution reflects changes in primary productivity and allochthonous biogenic material transported by icebergs, i.e. shell interval in GC3. The sharp Ba/Ti peaks found at ~137 cm and ~158 cm might instead indicate the establishment of a paleo SMTZ at some point after sediment deposition. Notably, localized barium enrichments can be indicators for paleo SMTZs (Argentino et al., 2021; Schneider et al., 2018; Yao et al., 2020). The dissolved barium is transported over the SMTZ as the fluids move upwards, and when it encounters sulfate-rich waters above the SMTZ, barite re-precipitates, forming a barite front (Carter et al., 2020; Torres et al., 1996). The sediment intervals in which we observe these barite enrichments are associated with very low TOC values (~0.2 %), and a remarkably negative $\delta^{13}C$ value in *C. wuellerstofi* was measured in the sediment interval hosting the upper barite front (Fig. 5a). Therefore, we interpret them as diagenetic fronts related to paleo-SMTZs. Two different barite fronts were identified in GC3 (i.e., Ba/Ti peaks at depths 158 cm and 137 cm), which we hereby define as paleo-SMTZ 1 and paleo-SMTZ 2, respectively (Fig. 3a). We speculate that the deeper barite front (paleo-SMTZ 1) was the first to have formed while the upper one (paleo-SMTZ 2) formed in more recent times. This is because older barite fronts tend to dissociate into barium and sulfate ions below the SMTZ. The Ba enrichment at 158 cm is smaller than the most recent one, possibly due to dissolution. It is not possible with the

available data to determine precisely when the first paleo-SMTZ established and when it migrated through the sediment column. We cannot speculate about the duration of the paleo-events recorded in GC3 since the formation of the geochemical anomalies, i.e. MDAC overgrowth on foraminifera and barite front, is influenced by various factors such as the fluid flow, AOM rates, ion availability (Feng et al., 2019; Karaca et al., 2010; Luff and Wallmann, 2003; Wang et al., 2018). We can only state that those events occurred later than the age of the sediments hosting the anomalies. Based on lithostratigraphic constraints, the sediments hosting the two barite fronts are older than Holocene ~11.7 cal ka BP and younger than the start of the Younger Dryas-post Bølling period ~14.5 cal ka BP. Therefore, we ascribe the time of barite front formation to later than ~14.5 cal ka BP. Additional investigations including radiocarbon dating will be useful to refine the age model for the sediment cores and paleo-seepage at Svyatogor Ridge. GC2 shows a few Ba/Ti spikes, single points that deviate from the adjacent values. Those signals are associated with irregularities on the surface of the split cores (Fig. 3b) so they do not correspond to true Ba enrichments but to artifacts.

However, the datasets reported in this study demonstrate for the first time that Svyatogor Ridge hosts an active methane seepage environment, with local hotspots of chemosynthesis sustained by anaerobic oxidation of methane. We found extreme spatial variability in the distribution of SMTZs, which indicates highly heterogeneous methane fluxes within the cold seep area. For instance, the cores PusC7 and BlaC3 were located only ~1 m from each other, but only BlaC3 showed the presence of a shallow SMTZ associated with a microbial mat at the seafloor. Moreover, owing to the dynamic nature of cold seeps, the conditions observed in this study only represent a snapshot of present-day processes and might vary in the future. Indeed, the presence of barite fronts buried >1 m below the seafloor in a core without signals of ongoing AOM, suggests a localized decrease of methane fluxes over time. These findings relate well with the previous studies at Svyatogor Ridge, indicating the presence of deep gas hydrate reservoirs and fluid flow systems (Waghorn et al., 2018), thus linking the deep subsurface with seafloor environments. The gas geochemistry points toward a primary microbial origin (Milkov and Etiope, 2018). The extremely negative $\delta^{13}C$ values recorded in the push cores (as low as $-85‰$) are consistent with the carbonate reduction pathway for gas formation. Methane seepage environments can be a common feature along active ultraslow-spreading ridges, which represent ca. 50% of the global mid-ocean ridge system and have only relatively recently been recognized to host hydrothermal activity(German et al., 1998). Therefore, our findings call for a reevaluation of the role of these ridges as potential areas of methane discharge into the ocean, encouraging further studies to explore the sources, distribution and magnitude of seepage and relationships with benthic ecosystems.

6. Conclusions

In this study, we report sediment and foraminiferal geochemistry data collected from different sediment cores from Svyatogor Ridge, a sediment-covered transform fault on the ultraslow-spreading mid-ocean ridge located to the west of Svalbard (Fram Strait). We provided biogeochemical evidence for ongoing anaerobic oxidation of methane in the shallow sedimentary column, with a sulfate-methane transition zone at ~6 cmbsf associated with microbial mats. We found two barite fronts buried deeper than 1 m below the seafloor, indicative of paleo-sulfate methane transitions. One barite front was associated with foraminiferal tests displaying a negative $\delta^{13}C$ value of $-12.73‰$, which reflects encrustation by methane-derived carbonate induced by past AOM. We ascribe the paleo-SMTZs to the Younger Dryas-post Bølling period (later than ~14.5 ka) according to chronostratigraphic constraints and modern pore water profiles. In our dataset, we also describe strong spatial heterogeneities in sediment biogeochemical processes, which ultimately reflect variations in the distribution of subsurface methane fluxes. The

cold seep environment reported in this study is sustained by methane fluxes conveyed toward the seafloor by underlying small-scale faults which serve as conduits for fluid flow (Waghorn et al., 2018). The gas geochemistry indicated a primary microbial origin for the seeping methane with $\delta^{13}C$ values as negative as $-85‰$. Our results provide the first evidence of methane seepage environment ever reported from the Arctic mid-ocean ridge, thus calling for a reevaluation of the role of ultraslow-spreading ridges in the ocean methane cycle and encouraging further investigations in these remote deep-sea settings.

CRediT authorship contribution statement

C. Argentino: Writing – original draft, Visualization, Supervision, Methodology, Investigation, Data curation, Conceptualization. **C. Borrelli:** Writing – review & editing, Supervision, Methodology, Investigation, Conceptualization. **A. Akinselure:** Writing – review & editing, Investigation, Formal analysis, Data curation. **M. Correa-Diaz:** Writing – review & editing, Investigation, Formal analysis. **G. Panieri:** Writing – review & editing, Supervision, Resources, Project administration, Methodology, Investigation, Funding acquisition, Conceptualization.

Declaration of competing interest

The authors declare the following financial interests/personal relationships which may be considered as potential competing interests:

Giuliana Panieri reports financial support was provided by Norges Forskiningsrad. If there are other authors, they declare that they have no known competing financial interests or personal relationships that could have appeared to influence the work reported in this paper.

Data availability

I have shared the data as supplementary material

Appendix A. Supplementary data

Supplementary data to this article can be found online at https://doi.org/10.1016/j.marpetgeo.2024.106761.

References

Argentino, C., Savini, A., Panieri, G., 2022a. Integrating fine-scale habitat mapping and pore water analysis in cold seep research: a case study from the SW Barents Sea. In: World Atlas of Submarine Gas Hydrates in Continental Margins. Springer International Publishing, Cham, pp. 505–514. https://doi.org/10.1007/978-3-030-81186-0_43.

Argentino, C., Lee, A., Fallati, L., Sahy, D., Birgel, D., Peckmann, J., Bünz, S., Panieri, G., 2022b. Biogeochemistry and timing of methane-derived carbonate formation at Leirdjupet fault complex, SW Barents sea. Front. Earth Sci. 10, 1–23. https://doi.org/10.3389/feart.2022.1029471.

Argentino, C., Waghorn, K.A., Vadakkepuliyambatta, S., Polteau, S., Bünz, S., Panieri, G., 2021. Dynamic and history of methane seepage in the SW Barents Sea: new insights from leirdjupet fault complex. Sci. Rep. 11, 4373. https://doi.org/10.1038/s41598-021-83542-0.

Berndt, C., Hensen, C., Mortera-Gutierrez, C., Sarkar, S., Geilert, S., Schmidt, M., Liebetrau, V., Kipfer, R., Scholz, F., Doll, M., Muff, S., Karstens, J., Planke, S.,

Petersen, S., Böttner, C., Chi, W.-C., Moser, M., Behrendt, R., Fiskal, A., Lever, M.A., Su, C.-C., Deng, L., Brennwald, M.S., Lizarralde, D., 2016. Rifting under steam—how rift magmatism triggers methane venting from sedimentary basins. Geology 44, 767–770. https://doi.org/10.1130/G38049.1.

Bernhard, J.M., Panieri, G., 2018. Keystone Arctic paleoceanographic proxy association with putative methanotrophic bacteria. Sci. Rep. 8, 10610 https://doi.org/10.1038/s41598-018-28871-3.

Boetius, A., Ravenschlag, K., Schubert, C.J., Rickert, D., Widdel, F., Gieseke, A., Amann, R., Jørgensen, B.B., Witte, U., Pfannkuche, O., 2000. A marine microbial consortium apparently mediating anaerobic oxidation of methane 407, 623–626. https://doi.org/10.1038/35036572.

Boetius, A., Wenzhöfer, F., 2013. Seafloor oxygen consumption fuelled by methane from cold seeps. Nat. Geosci. 6, 725–734. https://doi.org/10.1038/ngeo1926.

Bünz, S., Panieri, G., 2022. CAGE21-1 cruise report: AKMA-AKER-GReAT. CAGE – cent. Arct. Gas hydrate. Environ. Clim. Rep. Ser. 9 https://doi.org/10.7557/cage.6677.

Burley, J.M.A., Katz, R.F., 2015. Variations in mid-ocean ridge CO2 emissions driven by glacial cycles. Earth Planet Sci. Lett. 426, 246–258. https://doi.org/10.1016/j.epsl.2015.06.031.

Carter, S.C., Paytan, A., Griffith, E.M., 2020. Toward an improved understanding of the marine barium cycle and the application of marine barite as a paleoproductivity proxy. Minerals 10, 1–24. https://doi.org/10.3390/min10050421.

Consolaro, C., Rasmussen, T.L., Panieri, G., Mienert, J., Bünz, S., Sztybor, K., 2015. Carbon isotope (d13C) excursions suggest times of major methane release during the last 14 kyr in Fram Strait, the deep-water gateway to the Arctic. Clim. Past 11, 669–685. https://doi.org/10.5194/cp-11-669-2015.

Crémière, A., Lepland, A., Chand, S., Sahy, D., Condon, D.J., Noble, S.R., Martma, T., Thorsnes, T., Sauer, S., Brunstad, H., 2016. Timescales of methane seepage on the Norwegian margin following collapse of the Scandinavian Ice Sheet. Nat. Commun. 7, 1–10. https://doi.org/10.1038/ncomms11509.

Cruse, A.M., Seewald, J.S., 2006. Geochemistry of low-molecular weight hydrocarbons in hydrothermal fluids from Middle Valley, northern Juan de Fuca Ridge. Geochem. Cosmochim. Acta 70, 2073–2092. https://doi.org/10.1016/j.gca.2006.01.015.

Cui, Y., Kump, L.R., Ridgwell, A.J., Charles, A.J., Junium, C.K., Diefendorf, A.F., Freeman, K.H., Urban, N.M., Harding, I.C., 2011. Slow release of fossil carbon during the palaeocene–eocene thermal maximum. Nat. Geosci. 4, 481–485. https://doi.org/10.1038/ngeo1179.

Dessandier, P.-A.A., Borrelli, C., Yao, H., Sauer, S., Hong, W.-L.L., Panieri, G., 2020. Foraminiferal δ18O reveals gas hydrate dissociation in Arctic and North Atlantic ocean sediments. Geo Mar. Lett. 40, 507–523. https://doi.org/10.1007/s00367-019-00635-6.

Dessandier, P.A., Knies, J., Plaza Faverola, A., Labrousse, C., Renoult, M., Panieri, G., 2021. Ice-sheet melt drove methane emissions in the Arctic during the last two interglacials. Geology 49, 799–803. https://doi.org/10.1130/G48580.1.

Elverhøi, A., Andersen, E.S., Dokken, T., Hebbeln, D., Spielhagen, R., Svendsen, J.I., Sørflaten, M., Rørnes, A., Hald, M., Forsberg, C.F., 1995. The growth and decay of the late weichselian ice sheet in western svalbard and adjacent areas based on provenance studies of marine sediments. Quat. Res. 44, 303–316. https://doi.org/10.1006/qres.1995.1076.

Emerson, S., Hedges, J.I., 1988. Processes controlling the organic carbon content of open ocean sediments. Paleoceanography 3, 621–634. https://doi.org/10.1029/PA003i005p00621.

Etiope, G., Sherwood Lollar, B., 2013. Abiotic methane on Earth. Rev. Geophys. 51, 276–299. https://doi.org/10.1002/rog.20011.

Eynaud, F., 2011. Planktonic foraminifera in the Arctic: potentials and issues regarding modern and quaternary populations. IOP Conf. Ser. Earth Environ. Sci. 14, 012005 https://doi.org/10.1088/1755-1315/14/1/012005.

Feng, D., Qiu, J.-W., Hu, Y., Peckmann, J., Guan, H., Tong, H., Chen, C., Chen, J., Gong, S., Li, N., Chen, D., 2018. Cold seep systems in the South China Sea: an overview. J. Asian Earth Sci. 168, 3–16. https://doi.org/10.1016/j.jseaes.2018.09.021.

Feng, J., Yang, S., Wang, H., Liang, J., Fang, Y., Luo, M., 2019. Methane source and turnover in the shallow sediments to the west of haima cold seeps on the northwestern slope of the South China Sea. Geofluids 1–18. https://doi.org/10.1155/2019/1010824, 2019.

Ferré, B., Jansson, P.G., Moser, M., Serov, P., Portnov, A., Graves, C.A., Panieri, G., Gründger, F., Berndt, C., Lehmann, M.F., Niemann, H., 2020. Reduced methane seepage from Arctic sediments during cold bottom-water conditions. Nat. Geosci. 13, 144–148. https://doi.org/10.1038/s41561-019-0515-3.

Fischer, D., Sahling, H., Nöthen, K., Bohrmann, G., Zabel, M., Kasten, S., 2012. Interaction between hydrocarbon seepage, chemosynthetic communities, and bottom water redox at cold seeps of the Makran accretionary prism: insights from habitat-specific pore water sampling and modeling. Biogeosciences 9, 2013–2031. https://doi.org/10.5194/bg-9-2013-2012.

German, C.R., Baker, E.T., Mevel, C., Tamaki, K., 1998. Hydrothermal activity along the southwest Indian ridge. Nature 395, 490–493. https://doi.org/10.1038/26730 the FUJI Science Team.

Gilhooly, W.P., Carney, R.S., Macko, S.A., 2007. Relationships between sulfide-oxidizing bacterial mats and their carbon sources in northern Gulf of Mexico cold seeps. Org. Geochem. 38, 380–393. https://doi.org/10.1016/j.orggeochem.2006.06.005.

Grünke, S., Lichtschlag, A., De Beer, D., Felden, J., Salman, V., Ramette, A., Schulz-Vogt, H.N., Boetius, A., 2012. Mats of psychrophilic thiotrophic bacteria associated with cold seeps of the Barents Sea. Biogeosciences 9, 2947–2960. https://doi.org/10.5194/bg-9-2947-2012.

Hasenclever, J., Knorr, G., Rüpke, L.H., Köhler, P., Morgan, J., Garofalo, K., Barker, S., Lohmann, G., Hall, I.R., 2017. Sea level fall during glaciation stabilized atmospheric CO2 by enhanced volcanic degassing. Nat. Commun. 8 https://doi.org/10.1038/ncomms15867.

Heijs, S.K., Sinninghe Damsté, J.S., Forney, L.J., 2005. Characterization of a deep-sea microbial mat from an active cold seep at the Milano mud volcano in the Eastern Mediterranean Sea. FEMS Microbiol. Ecol. 54, 47–56. https://doi.org/10.1016/j.femsec.2005.02.007.

Hennekam, R., De Rick, G., 2012. X-ray fluorescence core scanning of wet marine sediments: methods to improve quality and reproducibility of highresolution paleoenvironmental records. Limnol Oceanogr. Methods 10, 991–1003. https://doi.org/10.4319/lom.2012.10.991.

Hensen, C., Zabel, M., Pfeifer, K., Schwenk, T., Kasten, S., Riedinger, N., Schulz, H.D., Boetius, A., 2003. Control of sulfate pore-water profiles by sedimentary events and the significance of anaerobic oxidation of methane for the burial of sulfur in marine sediments. Geochem. Cosmochim. Acta 67, 2631–2647. https://doi.org/10.1016/S0016-7037(03)00199-6.

Herguera, J.C., Paull, C.K., Perez, E., Ussler, W., Peltzer, E., 2014. Limits to the sensitivity of living benthic foraminifera to pore water carbon isotope anomalies in methane vent environments. Paleoceanography 29, 273–289. https://doi.org/10.1002/2013PA002457.

Himmler, T., Sahy, D., Martma, T., Bohrmann, G., Plaza-Faverola, A., Bünz, S., Condon, D.J., Knies, J., Lepland, A., 2019. A 160,000-year-old history of tectonically controlled methane seepage in the Arctic. Sci. Adv. 5, eaaw1450 https://doi.org/10.1126/sciadv.aaw1450.

Hoch, M.P., Fogel, M.L., Kirchman, D.L., 1992. Isotope fractionation associated with ammonium uptake by a marine bacterium. Limnol. Oceanogr. 37, 1447–1459. https://doi.org/10.4319/lo.1992.37.7.1447.

Hong, W.L., Torres, M.E., Carroll, J.L., Crémière, A., Panieri, G., Yao, H., Serov, P., 2017. Seepage from an arctic shallow marine gas hydrate reservoir is insensitive to momentary ocean warming. Nat. Commun. 8, 16126 https://doi.org/10.1038/ncomms16126.

Huybers, P., Langmuir, C., 2009. Feedback between deglaciation, volcanism, and atmospheric CO2. Earth Planet Sci. Lett. 286, 479–491. https://doi.org/10.1016/j.epsl.2009.07.014.

Huybers, P., Langmuir, C.H., 2017. Delayed CO2 emissions from mid-ocean ridge volcanism as a possible cause of late-Pleistocene glacial cycles. Earth Planet Sci. Lett. 457, 238–249. https://doi.org/10.1016/j.epsl.2016.09.021.

Jakubowicz, M., Agirrezabala, L.M., Dopieralska, J., Siepak, M., Kaim, A., Belka, Z., 2021. The role of magmatism in hydrocarbon generation in sedimented rifts: a Nd isotope perspective from mid-Cretaceous methane-seep deposits of the Basque-Cantabrian Basin, Spain. Geochem. Cosmochim. Acta 303, 223–248. https://doi.org/10.1016/j.gca.2021.03.025.

Johnson, J.E., Mienert, J., Plaza-faverola, A., Vadakkepuliyambatta, S., Knies, J., Bünz, S., Andreassen, K., Ferré, B., 2015. Abiotic Methane from Ultraslow-Spreading Ridges Can Charge Arctic Gas Hydrates, pp. 371–374. https://doi.org/10.1130/G36440.1.

Johnson, J.E., Phillips, S.C., Clyde, W.C., Giosan, L., Torres, M.E., 2021. Isolating detrital and diagenetic signals in magnetic susceptibility records from methane-bearing marine sediments. G-cubed 22, 1–21. https://doi.org/10.1029/2021GC009867.

Judd, A.G., Hovland, M., 2007. Seabed Fluid Flow: the Impact of Geology, Biology and the Marine Environment. https://doi.org/10.1007/s00254-004-1086-0.

Karaca, D., Hensen, C., Wallmann, K., 2010. Controls on authigenic carbonate precipitation at cold seeps along the convergent margin off Costa Rica. G-cubed 11, 1–19. https://doi.org/10.1029/2010GC003062.

Kasten, S., Zabel, M., Heuer, V., Hensen, C., 2003. Processes and signals of nonsteady-state diagenesis in deep-sea sediments and their pore waters. In: The South Atlantic in the Late Quaternary. https://doi.org/10.1007/978-3-642-18917-3_20.

Kennett, J.P., Cannariato, K.G., Hendy, I.L., Behl, R.J., 2000. Carbon isotopic evidence for methane hydrate instability during quaternary interstadials. Science 288, 128–133. https://doi.org/10.1126/science.288.5463.128.

Kienast, M., Higginson, M.J., Mollenhauer, G., Eglinton, T.I., Chen, M.-T., Calvert, S.E., 2005. On the sedimentological origin of down-core variations of bulk sedimentary nitrogen isotope ratios. Paleoceanography 20. https://doi.org/10.1029/2004PA001081.

Klasek, S.A., Hong, W.L., Torres, M.E., Ross, S., Hostetler, K., Portnov, A., Gründger, F., Colwell, F.S., 2021. Distinct methane-dependent biogeochemical states in Arctic seafloor gas hydrate mounds. Nat. Commun. 12, 1–13. https://doi.org/10.1038/s41467-021-26549-5.

Knies, J., Martinez, P., 2009. Organic matter sedimentation in the western Barents Sea region: terrestrial and marine contribution based on isotopic composition and organic nitrogen content. Nor. Geol. Tidsskr. 89, 79–89.

Konn, C., Charlou, J.L., Holm, N.G., Mousis, O., 2015. The production of methane, hydrogen, and organic compounds in ultramafic-hosted hydrothermal vents of the mid-atlantic ridge. Astrobiology 15, 381–399. https://doi.org/10.1089/ast.2014.1198.

Levin, L.A., Baco, A.R., Bowden, D.A., Colaco, A., Cordes, E.E., Cunha, M.R., Demopoulos, A.W.J.J., Gobin, J., Grupe, B.M., Le, J., Metaxas, A., Netburn, A.N., Rouse, G.W., Thurber, A.R., Tunnicliffe, V., Van Dover, C.L., Vanreusel, A., Watling, L., 2016. Hydrothermal vents and methane seeps: rethinking the sphere of influence. Front. Mar. Sci. 3, 1–23. https://doi.org/10.3389/fmars.2016.00072.

Lucchi, R.G., Camerlenghi, A., Rebesco, M., Colmenero-Hidalgo, E., Sierro, F.J., Sagnotti, L., Urgeles, R., Melis, R., Morigi, C., Bárcena, M.A., Giorgetti, G., Villa, G., Persico, D., Flores, J.A., Rigual-Hernández, A.S., Pedrosa, M.T., Macri, P., Caburlotto, A., 2013. Postglacial sedimentary processes on the Storfjorden and Kveithola trough mouth fans: significance of extreme glacimarine sedimentation. Global Planet. Change 111, 309–326. https://doi.org/10.1016/j.gloplacha.2013.10.008.

Luff, R., Wallmann, K., 2003. Fluid flow, methane fluxes, carbonate precipitation and biogeochemical turnover in gas hydrate-bearing sediments at Hydrate Ridge, Cascadia Margin: numerical modeling and mass balances. Geochem. Cosmochim. Acta 67, 3403–3421. https://doi.org/10.1016/S0016-7037(03)00127-3.

Macko, S.A., Fogel, M.L., Hare, P.E., Hoering, T.C., 1987. Isotopic fractionation of nitrogen and carbon in the synthesis of amino acids by microorganisms. Chem. Geol. Isot. Geosci. Sect. 65, 79–92. https://doi.org/10.1016/0168-9622(87)90064-9.

Madigan, M.T., Bender, K.S., Buckley, D.H., Sattley, M.W., Stahl, D.A., 2017. Brock Biology of Microorganisms, Global Edition, fifteenth ed. Pearson Education Limited.

Martin, R.A., Nesbitt, E.A., Campbell, K.A., 2010. The effects of anaerobic methane oxidation on benthic foraminiferal assemblages and stable isotopes on the Hikurangi Margin of eastern New Zealand. Mar. Geol. 272, 270–284. https://doi.org/10.1016/j.margeo.2009.03.024.

Maslov, A.V., Politova, N.V., Klyuvitkin, A.A., Kozina, N.V., Kravchishina, M.D., Novigatsky, A.N., Novichkova, E.A., Alekseeva, T.N., Shevchenko, V.P., 2023. Sources of material for surface bottom sediments in some regions of the nordic seas (based on geochemical data). Lithol. Miner. Resour. 58, 407–431. https://doi.org/10.1134/S0024490223700256.

Merdith, A.S., del Real, P.G., Daniel, I., Andreani, M., Wright, N.M., Coltice, N., 2020. Pulsated global hydrogen and methane flux at mid-ocean ridges driven by pangea breakup. G-cubed 21. https://doi.org/10.1029/2019GC008869.

Meyers, P.A., 1994. Preservation of elemental and isotopic source identification of sedimentary organic matter. Chem. Geol. 114, 289–302. https://doi.org/10.1016/0009-2541(94)90059-0.

Milkov, A.V., Etiope, G., 2018. Revised genetic diagrams for natural gases based on a global dataset of >20,000 samples. Org. Geochem. 125, 109–120. https://doi.org/10.1016/j.orggeochem.2018.09.002.

Millo, C., Sarnthein, M., Erlenkeuser, H., Frederichs, T., 2005. Methane-driven late Pleistocene $\delta^{13}C$ minima and overflow reversals in the southwestern Greenland Sea. Geology 33, 873. https://doi.org/10.1130/G21790.1.

Nelson, D.C., Waterbury, J.B., Jannasch, H.W., 1982. Nitrogen fixation and nitrate utilization by marine and freshwater Beggiatoa. Arch. Microbiol. 133, 172–177. https://doi.org/10.1007/BF00414997.

Panieri, G., 2006. Foraminiferal response to an active methane seep environment: a case study from the Adriatic Sea. Mar. Micropaleontol. 61, 116–130. https://doi.org/10.1016/j.marmicro.2006.05.008.

Panieri, G., Camerlenghi, A., Cacho, I., Cervera, C.S., Canals, M., Lafuerza, S., Herrera, G., 2012. Tracing seafloor methane emissions with benthic foraminifera: results from the ana submarine landslide (eivissa channel, western mediterranean sea). Mar. Geol. 291–294, 97–112. https://doi.org/10.1016/j.margeo.2011.11.005.

Panieri, G., Graves, C.A., James, R.H., 2016. Paleo-methane emissions recorded in foraminifera near the landward limit of the gas hydrate stability zone offshore western Svalbard. G-cubed 17, 521–537. https://doi.org/10.1002/2015GC006153.

Panieri, G., Lepland, A., Whitehouse, M.J., Wirth, R., Raanes, M.P., James, R.H., Graves, C.A., Crémière, A., Schneider, A., 2017. Diagenetic Mg-calcite overgrowths on foraminiferal tests in the vicinity of methane seeps. Earth Planet Sci. Lett. 458, 203–212. https://doi.org/10.1016/j.epsl.2016.10.024.

Rathburn, A.E., Levin, L.A., Held, Z., Lohmann, K.C., 2000. Benthic foraminifera associated with cold methane seeps on the northern California margin: ecology and stable isotopic composition. Mar. Micropaleontol. 38, 247–266. https://doi.org/10.1016/S0377-8398(00)00005-0.

Rathburn, A.E., Pérez, M.E., Martin, J.B., Day, S.A., Mahn, C., Gieskes, J., Ziebis, W., Williams, D., Bahls, A., 2003. Relationships between the distribution and stable isotopic composition of living benthic foraminifera and cold methane seep biogeochemistry in Monterey Bay, California. G-cubed 4. https://doi.org/10.1029/2003GC000595.

Ravelo, A.C., Hillaire-Marcel, C., 2007. Chapter eighteen the use of oxygen and carbon isotopes of foraminifera in paleoceanography. Dev. Mar. Geol. 1, 735–764. https://doi.org/10.1016/S1572-5480(07)01023-8.

Riedel, M., Villinger, H., Freudenthal, T., Pape, T., Bünz, S., Bohrmann, G., 2020. Thermal characterization of pockmarks across Vestnesa and svyatogor ridges. Offshore Svalbard. J. Geophys. Res. Solid Earth 125. https://doi.org/10.1029/2020JB019468.

Roberts, H.H., Feng, D., 2013. 3. Carbonate precipitation at gulf of Mexico hydrocarbon seeps: an overview. Hydrocarb. Seepage 43–61. https://doi.org/10.1190/1.9781560803119.ch3.

Rothwell, R.G., Croudace, I.w., 2015. Twenty Years of XRF Core Scanning Marine Sediments: what Do Geochemical Proxies Tell Us?, pp. 25–102. https://doi.org/10.1007/978-94-017-9849-5_2.

Ruby, E.G., Jannasch, H.W., Deuser, W.G., 1987. Fractionation of stable carbon isotopes during chemoautotrophic growth of sulfur-oxidizing bacteria. Appl. Environ. Microbiol. 53, 1940–1943. https://doi.org/10.1128/aem.53.8.1940-1943.1987.

Sahling, H., Rickert, D., Lee, R.W., Linke, P., Suess, E., 2002. Macrofaunal community structure and sulfide flux at gas hydrate deposits from the Cascadia convergent margin, NE Pacific. Mar. Ecol. Prog. Ser. 231, 121–138. https://doi.org/10.3354/meps231121.

Schneider, A., Crémière, A., Panieri, G., Lepland, A., Knies, J., 2017. Diagenetic alteration of benthic foraminifera from a methane seep site on Vestnesa Ridge (NW Svalbard). Deep. Res. Part I Oceanogr. Res. Pap. 123, 22–34. https://doi.org/10.1016/j.dsr.2017.03.001.

Schneider, A., Panieri, G., Lepland, A., Consolaro, C., Crémière, A., Forwick, M., Johnson, J.E., Plaza-Faverola, A., Sauer, S., Knies, J., 2018. Methane seepage at Vestnesa Ridge (NW svalbard) since the last glacial maximum. Quat. Sci. Rev. 193, 98–117. https://doi.org/10.1016/j.quascirev.2018.06.006.

Selley, R., Sonnenberg, S., 2015. Elements of Petroleum Geology. Elsevier. https://doi.org/10.1016/C2010-0-67090-8.

Sen Gupta, B.K., Platon, E., Bernhard, J.M., Aharon, P., 1997. Foraminiferal colonization of hydrocarbon-seep bacterial mats and underlying sediment, Gulf of Mexico slope. J. Foraminifer. Res. 27, 292–300. https://doi.org/10.2113/gsjfr.27.4.292.

Sinha, M.C., Evans, R.L., 2004. Geophysical constraints upon the thermal regime of the ocean crust. In: Geophysical Monograph Series, pp. 19–62. https://doi.org/10.1029/148GM02.

Svensen, H., Planke, S., Malthe-Sørenssen, A., Jamtveit, B., Myklebust, R., Rasmussen Eidem, T., Rey, S.S., 2004. Release of methane from a volcanic basin as a mechanism for initial Eocene global warming. Nature 429, 542–545. https://doi.org/10.1038/nature02566.

Torres, M.E., Brumsack, H.J., Bohrmann, G., Emeis, K.C., 1996. Barite fronts in continental margin sediments: a new look at barium remobilization in the zone of sulfate reduction and formation of heavy barites in diagenetic fronts. Chem. Geol. 127, 125–139. https://doi.org/10.1016/0009-2541(95)00090-9.

Torres, M.E., Martin, R.A., Klinkhammer, G.P., Nesbitt, E.A., 2010. Post depositional alteration of foraminiferal shells in cold seep settings: new insights from flow-through time-resolved analyses of biogenic and inorganic seep carbonates. Earth Planet Sci. Lett. 299, 10–22. https://doi.org/10.1016/j.epsl.2010.07.048.

Torres, M.E., Mix, A.C., Kinports, K., Haley, B., Klinkhammer, G.P., Mcmanus, J., Angelis, M.A. De, 2003a. Is methane venting at the seafloor recorded by D 13 C of benthic foraminifera shells ? 18, 1–13. https://doi.org/10.1029/2002PA000824.

Torres, M.E., Mix, A.C., Kinports, K., Haley, B., Klinkhammer, G.P., McManus, J., de Angelis, M.A., 2003b. Is methane venting at the seafloor recorded by δ 13 C of benthic foraminifera shells? Paleoceanography 18. https://doi.org/10.1029/2002PA000824.

Wada, E., 1980. Nitrogen isotope fractionation and its significance in biogeochemical processes occurring in marine environments. Isot. Mar. Chem. 375–398.

Waghorn, K.A., Bünz, S., Plaza-Faverola, A., Johnson, J.E., 2018. 3-D seismic investigation of a gas hydrate and fluid flow system on an active Mid-Ocean Ridge; Svyatogor Ridge, Fram Strait. G-cubed 19, 2325–2341. https://doi.org/10.1029/2018GC007482.

Waghorn, K.A., Vadakkepuliyambatta, S., Plaza-Faverola, A., Johnson, J.E., Bünz, S., Waage, M., 2020. Crustal processes sustain Arctic abiotic gas hydrate and fluid flow systems. Sci. Rep. 10, 1–14. https://doi.org/10.1038/s41598-020-67426-3.

Wang, X., Li, N., Feng, D., Hu, Y., Bayon, G., Liang, Q., Tong, H., Gong, S., Tao, J., Chen, D., 2018. Using chemical compositions of sediments to constrain methane seepage dynamics: a case study from Haima cold seeps of the South China Sea. J. Asian Earth Sci. 168, 137–144. https://doi.org/10.1016/j.jseaes.2018.11.011.

Welhan, J.A., 1988. Origins of methane in hydrothermal systems. Chem. Geol. 71, 183–198. https://doi.org/10.1016/0009-2541(88)90114-3.

Wong, K., Mason, E., Brune, S., East, M., Edmonds, M., Zahirovic, S., 2019. Deep carbon cycling over the past 200 million years: a review of fluxes in different tectonic settings. Front. Earth Sci. 7, 1–22. https://doi.org/10.3389/feart.2019.00263.

Wu, L., Wilson, D.J., Wang, R., Yin, X., Chen, Z., Xiao, W., Huang, M., 2020. Evaluating Zr/Rb ratio from XRF scanning as an indicator of grain-size variations of glaciomarine sediments in the southern ocean. G-cubed 21. https://doi.org/10.1029/2020GC009350.

Yao, H., Niemann, H., Panieri, G., 2020. Multi-proxy approach to unravel methane emission history of an Arctic cold seep. Quat. Sci. Rev. 244, 106490 https://doi.org/10.1016/j.quascirev.2020.106490.

Zachos, J.C., Röhl, U., Schellenberg, S.A., Sluijs, A., Hodell, D.A., Kelly, D.C., Thomas, E., Nicolo, M., Raffi, I., Lourens, L.J., McCarren, H., Kroon, D., 2005. Paleoclimate: rapid acidification of the ocean during the paleocene-eocene thermal maximum. Science 80. https://doi.org/10.1126/science.1109004.

Zhuang, G., Montgomery, A., Sibert, R.J., Rogener, M., Samarkin, V.A., Joye, S.B., 2018. Effects of pressure, methane concentration, sulfate reduction activity, and temperature on methane production in surface sediments of the Gulf of Mexico. Limnol. Oceanogr. 63, 2080–2092. https://doi.org/10.1002/lno.10925.